Research Article

Trailblazing Kr/Xe Separation: The Birth of the First Kr-Selective Material

Mona H. Mohamed,* Islam Elzeny, Joshua Samuel, Yimeng Huang, Ahmed S. Helal, Mitchell Galanek, Wenqian Xu, So Yeon Kim, Tony Pham, Lenore Miller, Adam Hogan, Brian Space, Ju Li, and Sameh K. Elsaidi*

Read Online

ACCESS | Metrics & More | Article Recommendations | SI Supporting Information

ABSTRACT: Efficient separation of Kr from Kr/Xe mixtures is pivotal in nuclear waste management and dark matter research. Thus far, scientists have encountered a formidable challenge: the absence of a material with the ability to selectively adsorb Kr over Xe at room temperature. This study presents a groundbreaking transformation of the renowned metal−organic framework (MOF) CuBTC, previously acknowledged for its Xe adsorption affinity, into an unparalleled Kr-selective adsorbent. This achievement stems from an innovative densification approach involving systematic compression of the MOF, where the crystal size, interparticle interaction, defects, and evacuation conditions are synergistically modulated. The resultant densified CuBTC phase exhibits exceptional mechanical resilience, radiation tolerance, and notably an unprecedented selectivity for Kr over Xe at room temperature. Simulation and experimental kinetic diffusion studies confirm reduced gas diffusion in the densified MOF, attributed to its small pore window and minimal interparticle voids. The lighter Kr element demonstrates facile surface passage and higher diffusivity within the material, while the heavier Xe encounters increased difficulty entering the material and lower diffusivity. This Kr-selective MOF not only represents a significant breakthrough in Kr separation but also demonstrates remarkable processability and scalability to kilogram levels. The findings presented herein underscore the transformative potential of engineered MOFs in addressing complex challenges, heralding a new era of Kr separation technologies.
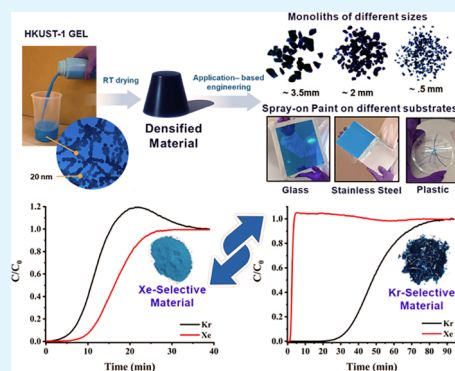
■ INTRODUCTION

Efficiently separating Kr from Kr/Xe mixtures holds paramount importance in critical applications, such as nuclear waste management and the detection of dark matter.[1−4] Within nuclear reactor operations, Xe and Kr emerge as byproducts and the failure to separate these gases poses potential threats to the environment. Moreover, Xe serves as a principal target gas in dark matter detectors, yet commercially sourced Xe invariably contains Kr impurities, compromising the precision and sensitivity of dark matter investigations.[5,6] Currently, cryogenic distillation is employed for Xe and Kr separation, a technique which unfortunately necessitates extremely low temperatures, thereby escalating both the complexity and cost associated with the process.[7,8] Various solid adsorbents, including activated carbons, zeolites, and metal−organic frameworks (MOFs), have been utilized to separate these gases more efficiently.[9,10] However, existing solid-state adsorbents predominantly favor Xe adsorption over Kr at room temperatures due to the higher boiling point and polarizability of Xe. As a result, the adsorbent materials quickly reach saturation due to substantial concentrations of Xe, which are at least 10 times higher than those of Kr. This leads to significant time gaps during the separation process.

Logically, the most promising approach to address these challenges is the development of a material adept at selectively separating Kr from Kr/Xe mixtures. Theoretically, ultra-microporous adsorbents could favor Kr capture through a molecular sieving mechanism, considering the larger kinetic diameter of Xe (4.1 Å) compared to Kr (3.6 Å). MOFs, with their adjustable pore structures, have emerged as ideal candidates for implementing this strategy. However, current microporous MOFs exhibit an inverse size-sieving property, favoring Xe adsorption due to their strong interaction with Xe or the framework flexibility. For example, our efforts to design Kr-selective ultramicroporous MOFs (with approximately 3.6 Å pore size) were thwarted as the materials continued to prefer Xe, attributed to the higher affinity of the MOF for Xe and
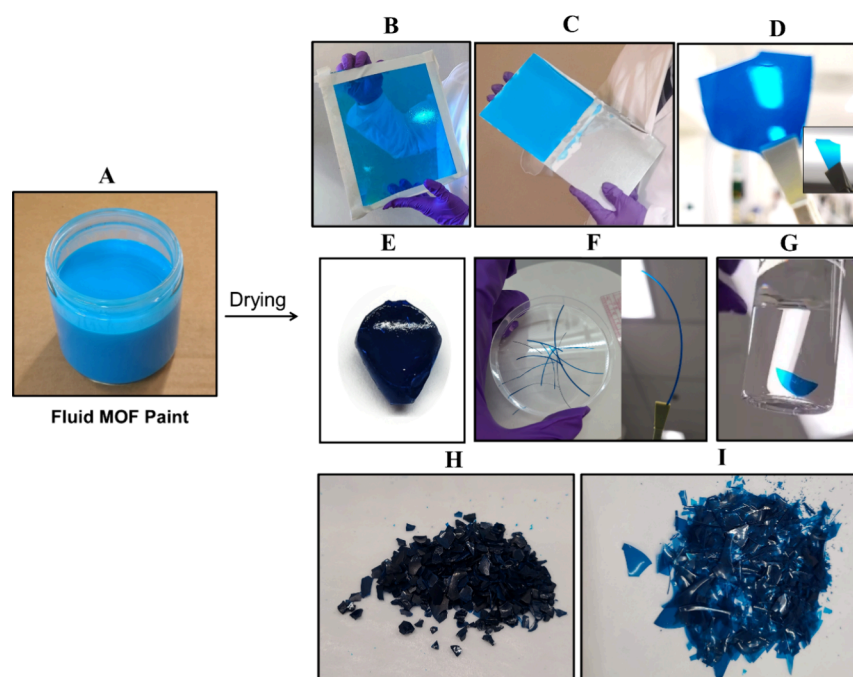
Figure 1. Pictures of the different forms of densified material. (A) Gel CuBTC in ethanol. (B) Thin film coated on a 30 cm glass sheet. (C) Thin film coated on a 20 cm stainless steel sheet. (D) Transparent self-standing sheets. (E) A monolithic chuck as a size of a quarter. (F) Self-standing strands after being taken out of silicon molds. (G) Stability of the sheet after shaking and soaking in ethanol for a month. (H, I) Scale-up of Mono-CuBTC and FS-CuBTC, respectively.

augmented framework flexibility facilitated by benzene ring rotations in the ligands, providing additional space for Xe adsorption.[11−13] In this study, we unveil a groundbreaking achievement—the development of the first-ever adsorbent material that selectively adsorbs Kr over Xe under ambient conditions. This significant breakthrough is realized by adeptly controlling the diffusion of gases into the MOF framework by leveraging the inherent differences in diffusivity between Xe and Kr.

In our quest to master gas diffusion control in MOFs, we endeavor to optimize nanoparticle packing during the MOF densification process, strategically establishing a diffusion barrier on the MOF surface. For this study, the CuBTC MOF (BTC referring to 1,3,5-benzene tricarboxylic acid or trimesic acid)[14] was chosen due to its well-documented properties, including modifiable particle size, manageable defect formation, stability, and facile synthesis and activation methods. Unlike previous approaches relying on pressure or additives for CuBTC densification, our objective was to control the packing of MOF particles without using binders or pressure.[15−17] We have recently introduced an innovative strategy for MOF densification, combining three effective techniques to synergistically enhance particle packing during the densification of CuBTC MOF.[18] First, we reduced the size of the MOF nanoparticles, significantly improving their close packing. Second, defects were introduced into the copper paddlewheel clusters within the MOF structure, promoting chemical interactions between neighboring particles during the drying process. Third, vacuum-induced stress was applied to eliminate any remaining interparticle spaces, further enhancing the compactness of the framework. This strategic process initially forms a gel-like material of CuBTC MOF, suspended in ethanol and resembling fluid paint. The nanoparticles suspended in ethanol showed a size range between 20 and 60 nm, as observed using

transmission electron microscopy (TEM), as shown in Figure S5. The gel-like material offers versatility in application through commercial paint sprayers or casting onto various surfaces such as stainless steel, glass, and plastics by using knife or drop-casting techniques. Upon drying, it forms continuous coatings, as visually demonstrated in Video S1. Our developed material can be shaped into monolithic chunks with different sizes, strands, or self-standing flat sheets, adaptable to various containers by transferring the gel-like substance into different molds and allowing it to solidify (Figure 1 and Figures S1−S3). This unique capability surpasses the characteristics of many monolithic substances, which often require high-speed centrifugation for densification. Remarkably, the gel-like formulation consistently achieves a densified form, in contrast to the powder material, which fails to densify under similar conditions (Figure S4). We successfully synthesized a powdered form of the material, termed CuBTC$_{TWP}$, by subjecting the gel-like product to a thorough washing process. This step underscores our hypothesis, as rigorous washing removes any unreacted species on the surface, which are the driving force behind the creation of the highly densified material.

In this study, we cast a spotlight on two forms of densified CuBTC: monolith (Mono-CuBTC) and flat sheets (FS-CuBTC). Mono-CuBTC is formed by allowing the centrifuged, gel-like nanoparticles to dry in a centrifuge tube, while FS-CuBTC is created by uniformly dispersing the gel-like substance across a glass surface to dry. The surface areas of the materials were evaluated for the materials activated at 150 °C for 12 h by collecting the N$_2$ adsorption isotherms at 77K. The Brunauer−Emmett−Teller (BET) surface area (SA) of CuBTC$_{TWP}$, Mono-CuBTC, and FS-CuBTC were 1406, 769, and 775 m^2 g$^{−1}$, respectively (see Figures S9−S11). Both Mono-CuBTC and FS-CuBTC displayed lower SAs compared with the powder form. This may be attributed to the high density of the materials,

resulting in a lower volumetric uptake. The experimentally derived skeletal densities (Figures S6−S8) of Mono-CuBTC and FS-CuBTC were found to be 2.55 and 1.9 g cm^{-3}, respectively, exhibiting significantly higher density values compared to the density of TWP (1.32 g cm^{-3}). In this regard, CuBTC$_{TWP}$ exhibited a bulk density of 0.7 g cm^{-3}, representing only 58% of the theoretical CuBTC density, which is 1.2 g cm^{-3}. The highest density value reported previously for densified CuBTC attains only 88% of the crystallographic density.[19] Based on the pore volumes of 0.37 and 0.40 cm^3 g^{-1}, the bulk densities of Mono-CuBTC (SA = 769) and FS-CuBTC (SA = 775) are 1.3 and 1.1 g cm^{-3}, which correlate with 108 and 92% of crystallographic density, respectively, indicating attainable values surpassing 100% of the crystal density. This is compelling proof that the densification process reduces not only interparticle voids but also internal porosity while increasing the bulk density.

The introduction of defects within a MOF structure can indeed foster a degree of flexibility in the framework by combining both rigid and nonrigid walls into the MOF structure.[20−30] This flexibility can potentially be modulated through the densification process of the MOF nanoparticles, influencing both the pore characteristics and the separation performance of the material. In theory, there are very minimal or negligible voids between the particles after the densification process with the only remaining free volume being harbored within the intrinsic porosity of the substance. Hence, it is plausible that any further densification would exert a direct influence on the internal pores, representing the sole remaining void spaces within the material. This particular behavior has been witnessed in our densification trajectory of CuBTC.[18]

Therefore, we studied the impact of a vacuum as an external stimulant on densified MOF flexibility and adsorption properties. Samples from the same batch of the Mono-CuBTC underwent vacuum activation at 150 °C for a 12 h period, followed by further activations at 25 °C for different time intervals. The Mono-CuBTC material displayed a gradual decline in N$_2$ uptake, BET SA, and pore volume as the duration of vacuum exposure increased (Figures S12 and S13 and Table S1). Specifically, the BET SAs decreased from 769 m^2/g for samples subjected to no extended vacuum to 528 and 377 m^2/g for samples subjected to further vacuum durations of 1 and 2 days, respectively. Ultimately, the material exhibited no measurable SA after prolonged vacuum exposure lasting 5−6 days (as depicted in Figures S12 and S13). A similar trend was noted for FS-CuBTC, as shown in Figures S14 and S15. The N$_2$ adsorption isotherms acquired at 77 K demonstrated mixed type I/IV behavior. Although the observed hysteresis suggested the presence of mesoporosity due to defects, analysis of the NLDFT pore size distribution revealed minimal contribution from mesoporosity in the densified material, with the majority of pores being micropores. In contrast, CuBTC$_{TWP}$ exhibited mesopores (>10 nm), likely arising from the formation of larger cavities due to the removal of BTC units during thorough washing. Notably, analysis using the Horvath−Kawazoe method for micropore size indicated a reduction in pore diameter with increasing vacuum activation times of 12 h, 2 days, and 4 days, as illustrated in Figure S16. The application of vacuum-induced strain on the CuBTC structure, leading to impairment of its structure and internal pores, further exacerbating the observed decrease in SA and pore volume in both Mono-CuBTC and FS-CuBTC samples.

In an effort to comprehend this behavior, we conducted powder-X-ray diffraction (PXRD). The Pawley refinement of PXRD confirmed the presence of peak splitting and shifts in the Mono-CuBTC and FS-CuBTC samples activated for a longer duration compared to the as-synthesized analogue and the simulated pattern (Figures S17 and S18). The data revealed that the lattice symmetry is reduced from cubic to tetragonal in both forms, validating that the framework undergoes a drastic shearing process to minimize the void space within the structure (Table 1). This shearing process leads to a downsizing of the

Table 1. Lattice Parameters Obtained from Pawley Refinement

MOF	crystal system	a (Å)	c (Å)	volume (Å^3)
reported CuBTC	cubic	26.271(1)	26.271(1)	18132(2)
CuBTC$_{TWP}$	cubic	26.269(1)	26.269(1)	18128(2)
Mono-CuBTC$_{UM}$	tetragonal	18.859(2)	25.365(6)	9022(3)
FS-CuBTC$_{UM}$	tetragonal	18.807(2)	25.287(4)	8944(3)

pores, resulting in the formation of ultramicroporous (UM) CuBTC variants, namely, Mono-CuBTC$_{UM}$ and FS-CuBTC$_{UM}$. Defects in these materials were confirmed using proton nuclear magnetic resonance (^{1}HNMR). The appearance of peaks corresponding to the three methyl protons in acetate at 1.86 ppm, along with peaks attributed to the BTC linker in the ^{1}HNMR spectra, clearly indicated the presence of acetate fragments within the FS-CuBTC$_{UM}$ structure (see Figure S19). This analysis revealed a BTC:acetate ratio of approximately 3:1. In contrast, the ^{1}H NMR spectrum of activated CuBTC$_{TWP}$ showed a distinct signal from BTC ligands, with no detectable signals from acetate. While Mono-CuBTC$_{UM}$ and FS-CuBTC$_{UM}$ exhibited no specific SA, they demonstrated CO$_2$ uptakes at 298 K comparable to those of CuBTC$_{TWP}$ (Figures S20 and S21). This specific observation serves as a positive indication of the maintained porosity of these materials at room temperature. Given these facts, it is pivotal to consider the role of gas diffusion within these structures, a phenomenon fundamentally altered with the downsizing of pore dimensions. In MOF with large pores, the diffusion of gases is almost equally and unhampered, with the adsorption dynamics and selectivity largely hinging on the interactions between the gas and the framework structure. However, the narrative shifts significantly with the advent of narrowed pore dimensions, as seen in the case of Mono-CuBTC$_{UM}$ and FS-CuBTC$_{UM}$. In this context, gas diffusion encounters considerable hindrance due to the spatially confined dimensions and, more importantly, hindrance at the surface due to the minimal gaps between particles, thereby amplifying selectivity toward gases capable of navigating through these pores freely. This diffusion barrier is most prominent at lower temperatures. At 77K, it is observed that the gas can no longer diffuse into the pores of Mono-CuBTC$_{UM}$ and FS-CuBTC$_{UM}$ because it lacks sufficient kinetic energy to surmount the diffusion barrier imposed by the confined space, as previously observed in MOFs with ultramicropores.[31−33]

Considering the inherent difference in diffusivity between Xe and Kr, we hypothesized that these densified materials would be ideal candidates for the selective capture of Kr from Kr/Xe gas mixtures. To test this hypothesis systematically, we performed Xe and Kr adsorption using the following samples: CuBTC$_{TWP}$, Mono-CuBTC (769), and Mono-CuBTC (377), and Mono-CuBTC$_{UM}$ (numerical BET SA value indicated in parentheses
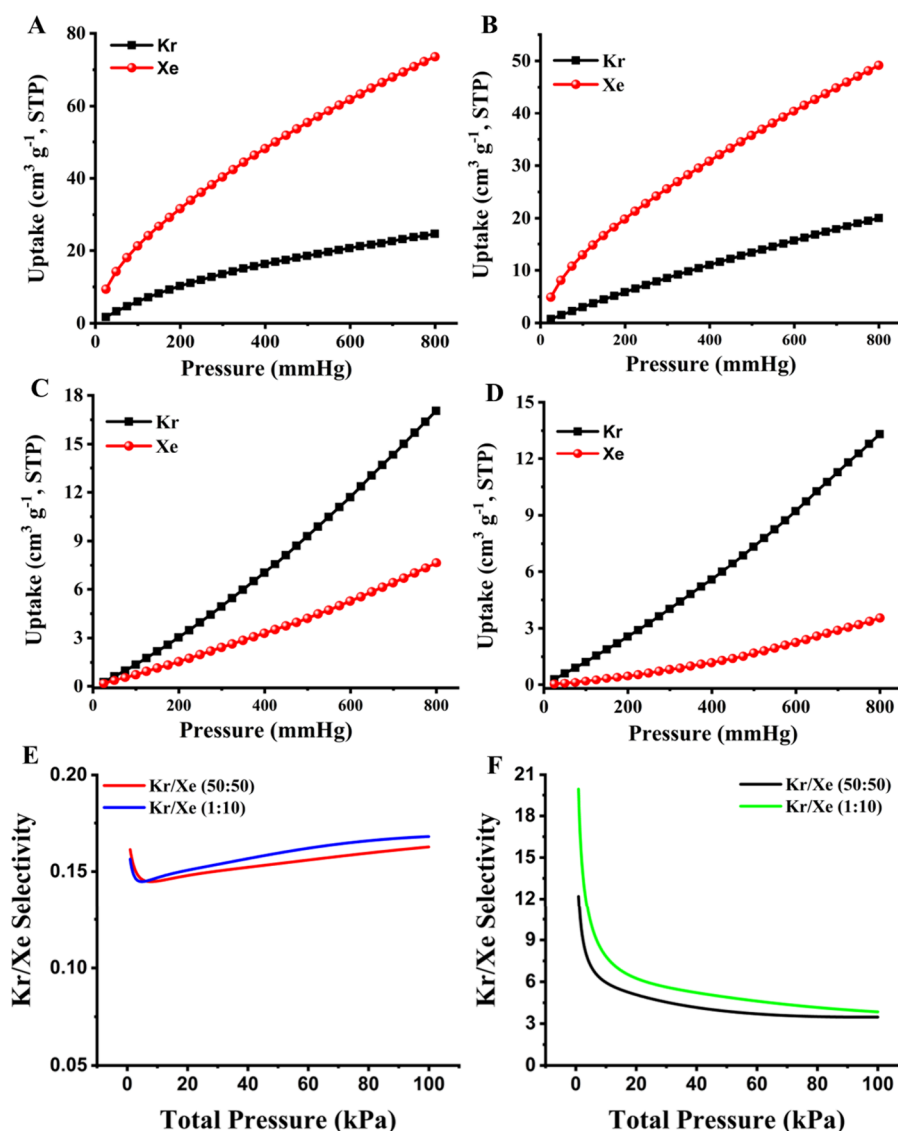
Figure 2. Single Kr and Xe adsorption isotherms and IAST selectivity at 298 K. (A) Kr and Xe isotherms of CuBTC$_{TWP}$. (B) Kr and Xe isotherms of Mono-CuBTC (769). (C) Kr and Xe isotherms of Mono-CuBTC$_{UM}$. (D) Kr and Xe isotherms of FS-CuBTC$_{UM}$. (E) Kr/Xe selectivity of CuBTC$_{TWP}$. (F) Kr/Xe selectivity of FS-CuBTC$_{UM}$.

while the UM variant showed no SA). Both CuBTC$_{TWP}$ and Mono-CuBTC (769) demonstrated preferential adsorption of Xe over Kr, albeit the latter exhibited diminished uptake values for both Xe and Kr, a consequence of its reduced SA (Figure 2A,B). Interestingly, starting in Mono-CuBTC (377), the selectivity was reversed with Kr selectively adsorbed over Xe while the diffusion of Xe was restricted at this point (Figure S22). Ideal Adsorbed Solution Theory (IAST) calculations revealed that Mono-CuBTC (377) exhibits Kr over Xe selectivity at 1 bar and 298 K of 1.52 and 1.54 for 1:1, and 1:10 Kr/Xe gas mixtures, respectively (Figure S23), while corresponding IAST Kr/Xe selectivities of CuBTC$_{TWP}$ were found to be only 0.16 and 0.17, respectively (Figure 2E). Following this, we postulated that with a further increase in the vacuum time CuBTC$_{UM}$ could have even further enhanced Kr selectivity. As expected, the Mono-CuBTC$_{UM}$, kept under vacuum for longer time showed an enhanced Kr/Xe selectivity of 1.9 (Figure 2C and Figure S24). We anticipated that the FS-CuBTC$_{UM}$ will exhibit behavior analogous to that of the Mono-CuBTC$_{UM}$ since they were prepared from the same batch.

However, the FS-CuBTC$_{UM}$ showed superior IAST Kr/Xe selectivity of 3.5 and 3.8 for 1:1, and 1:10 Kr/Xe gas mixtures, respectively, compared to Mono-CuBTC$_{UM}$ (Figure 2D,F). This could be attributed to the consistent nanocrystal packing on the glass surface of FS-CuBTC compared to Mono-CuBTC. This enhanced packing quality potentially eases the densification process and pore compression during the drying stage, consequently fostering an enhanced Kr selectivity. These are the first set of materials to selectively adsorb Kr over Xe at ambient temperature and pressure. Prior to this, only two studies documented a separation favoring Kr over Xe, albeit necessitating a significantly low operating temperature, thereby limiting its practical applicability.[34,35] Other reports presented computational studies on potential candidates for Kr-selective materials, but these theoretical results are yet to be verified experimentally.[36,37] Thus, to the best of our knowledge, no previously investigated MOF or other solid adsorbent has experimentally demonstrated the ability to selectively adsorb Kr over Xe at ambient temperature and pressure, marking a significant milestone in this realm of research.
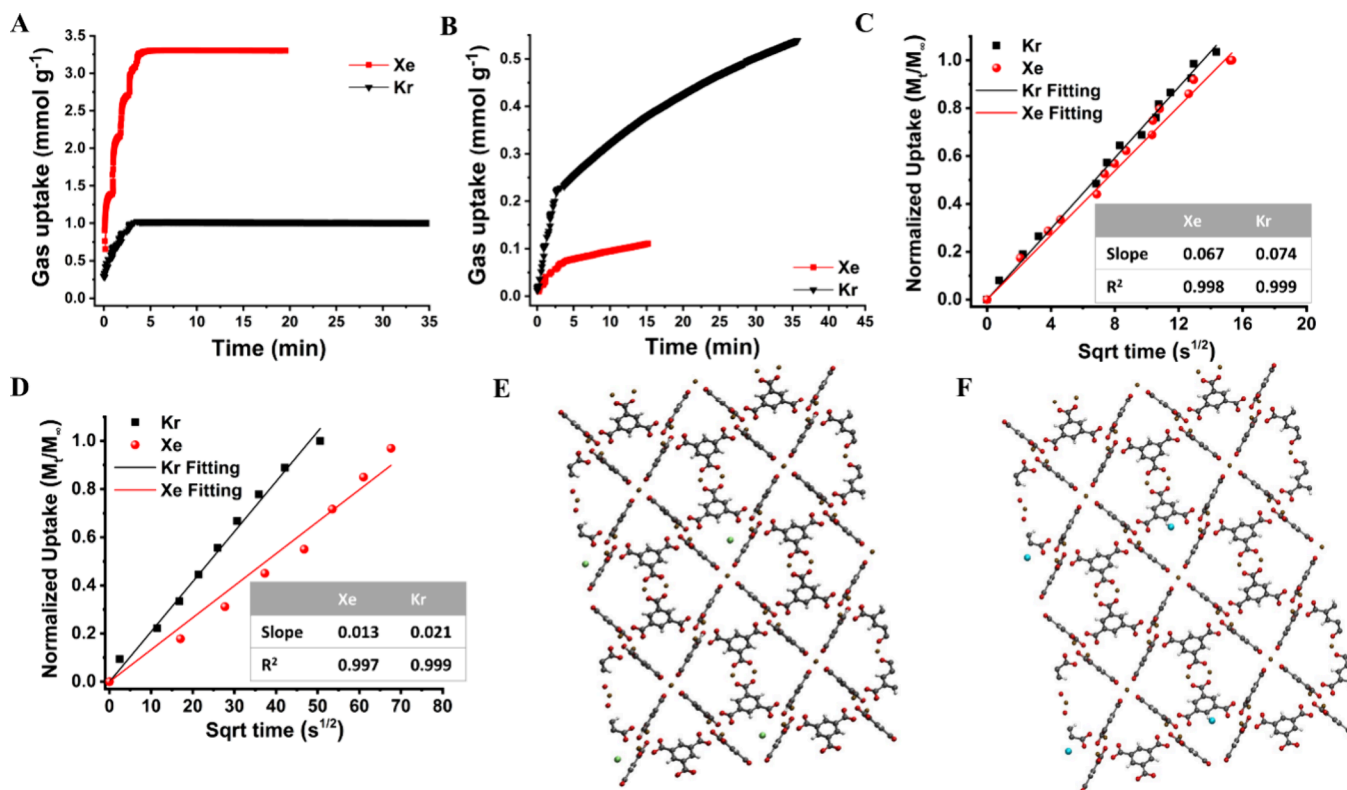
Figure 3. Diffusion and simulation studies. Time-dependent gas uptake profiles of Xe, and Kr at 1 bar and 298 K in CuBTC$_{TWP}$ (A) and FS-CuBTC$_{UM}$ (B). Details for the calculation of the diffusional time constant for experimental Xe and Kr diffusion in CuBTC$_{TWP}$ (C) and FS-CuBTC$_{UM}$ (D) at 298 K and 1 bar. Kr (green, E) and Xe (blue, F) in the FS-CuBTC$_{UM}$ MOF. These images were taken at the same time in the simulation, and Xe consistently spent more time in the tetragonal pore than did Kr.
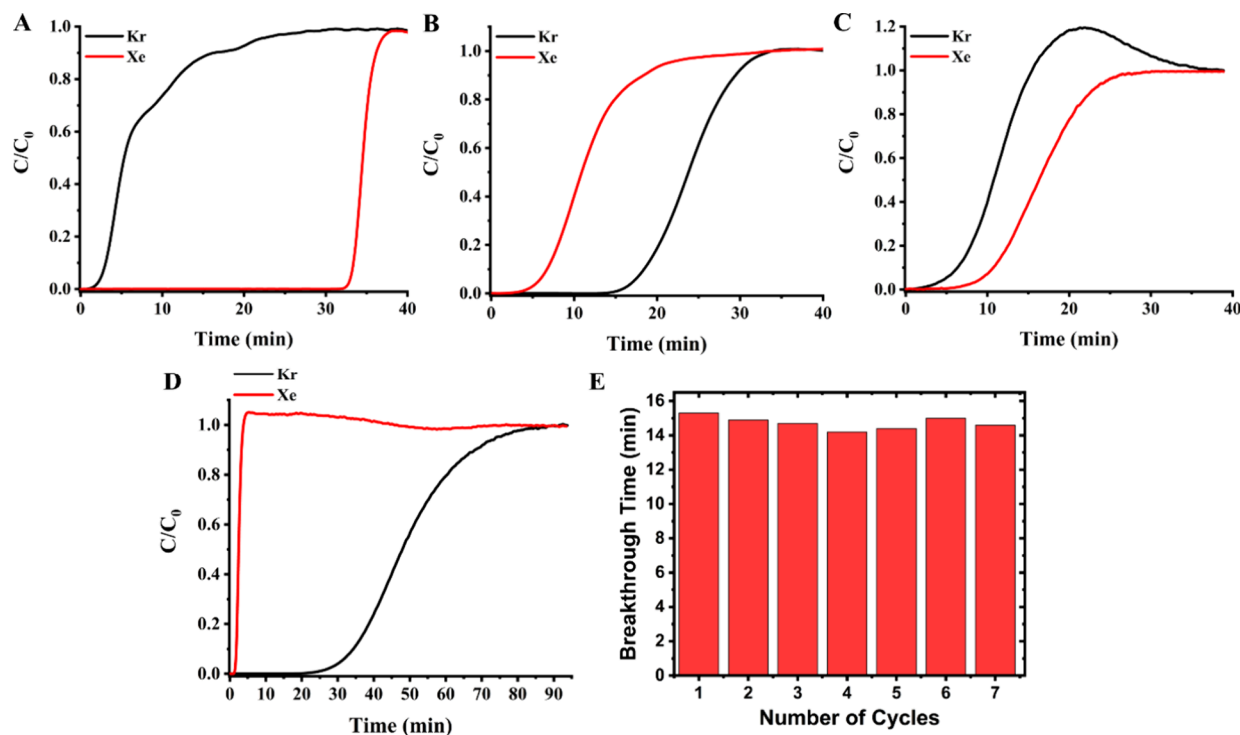
Figure 4. Column breakthrough experiments for different Xe and Kr gas mixtures. Breakthrough curves of 1:1 Kr/Xe mixture for (A) CuBTC$_{TWP}$ and (B) FS-CuBTC$_{UM}$. Breakthrough curves of 1:10 Kr/Xe mixture for (C) CuBTC$_{TWP}$ and (D) FS-CuBTC$_{UM}$. (E) Cycle dynamic tests were collected using breakthrough experiments of the 1:1 Kr/Xe mixture with a packed bed of FS-CuBTC$_{UM}$.
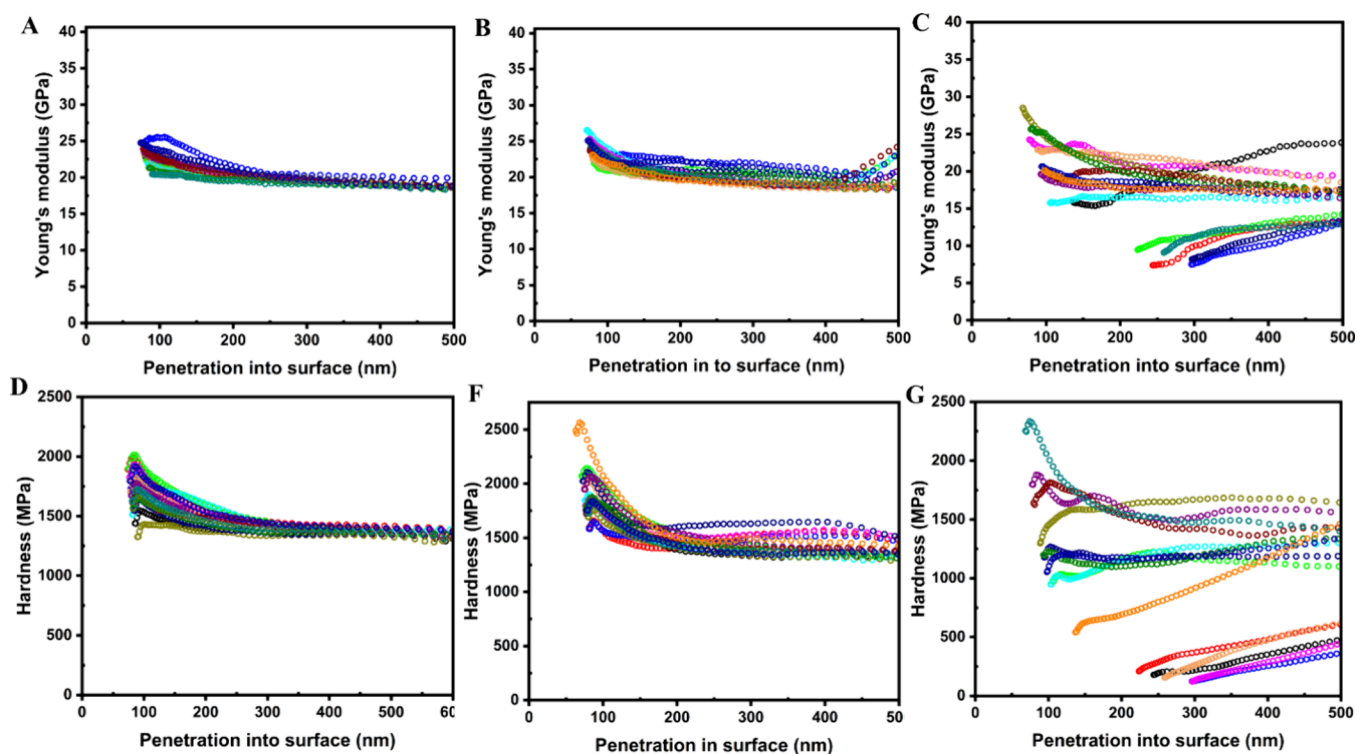
Figure 5. Nanoindentation study before and after radiation. Young's modulus of FS-CuBTC$_{UM}$ (A) before irradiation, (B) after irradiation at 800 kGy, and (C) after irradiation at 1000 kGy. Hardness of FS-CuBTC$_{UM}$, (D) before irradiation, (F) after irradiation at 800 kGy, and (G) after irradiation at 1000 kGy.

The isosteric heats of adsorption (Q_{st}) provide valuable insights into the thermodynamic aspects of the adsorption processes. For comparison, we calculate the Q_{st} values for Xe and Kr adsorbed onto Mono-CuBTC (769) (Xe-selective) and Mono-CuBTC$_{UM}$ (Kr-selective) at 298 and 273 K using the virial method (Figure S25−S28). As expected, due to Xe higher polarizability compared to Kr, the Q_{st} values for Xe are higher than those for Kr (Figures S29 and S30) in Mono-CuBTC (769). These values are initially higher at low loading and gradually decrease with increasing loading, consistent with the behavior of materials featuring open metal centers. In Mono-CuBTC$_{UM}$, Kr exhibits exothermic enthalpy values (Figure S31) that increase with higher Kr loadings, indicating attractive intermolecular interactions between the framework and Kr at elevated Kr loading levels. However, we observe peculiar behavior in Xe enthalpies of adsorption. As the temperature decreases, Xe uptakes also decrease and enthalpy values as a function of Xe loading remain consistently positive, indicating endothermic behavior during Xe adsorption (Figure S32). Particularly, these positive values are higher at low loadings, suggesting that Xe adsorption by Mono-CuBTC$_{UM}$ presents challenges. Nonetheless, with increasing Xe loading, the positive enthalpy values decrease. This unexpected outcome may be attributed to the larger size of Xe molecules, resulting in slower diffusion into framework cavities compared to smaller Kr molecules. Conducting these calculations with FS-CuBTC$_{UM}$ poses challenges as the material cannot adsorb Xe and Kr at low temperatures due to its "kinetically closed pore" nature. Gas diffusion into these ultramicropores is hindered at low temperatures unless the gas possesses sufficient kinetic energy to overcome the diffusion barrier.

The findings call for a more thorough investigation of the kinetic adsorption characteristics of these materials. The time-dependent uptake was observed for FS-CuBTC$_{UM}$ and CuBTC$_{TWP}$ to scrutinize the diffusion of gases from the bulk to the pores of the materials. The diffusional time constants, D', can be obtained for Xe and Kr gases by calculating the slope of the line as shown in Figure 3A−D. The findings reveal that FS-CuBTC$_{UM}$ demonstrates a swifter diffusion rate for Kr compared to Xe (8.7×10^{-5} vs 3.3×10^{-5} s^{-1}). This establishes FS-CuBTC$_{UM}$ as a Kr-preferential adsorbent in terms of kinetic factors, showcasing the resistance to Xe diffusion. Conversely, CuBTC$_{TWP}$ displays a comparable diffusional time constant for both gases (1.0×10^{-3} vs 8.9×10^{-4} s^{-1}). These results underscore that the intricacies of the densification process governing the diffusion between particles, which restricts gas diffusion from the bulk to the pore and the reduced pore size, which hinders gas diffusion from the surface into the internal pores, can profoundly influence the selectivity of these gases.

For further exploration, simulations were conducted in the NVT ensemble at a temperature of 298 K and a time step of 2 fs using OpenMM 8.0. Both sorbates and the MOF were parametrized with the PHAST2 force field, encompassing explicit induced dipole polarization (Figures 3E to Figure 4F). Experimental crystal structures were employed by assuming the MOF to be rigid. There were many effects the simulation could not easily capture, specifically the surface interactions both gases would need to pass through to reach the bulk of the material. CuBTC$_{TWP}$ offers more SA for gases to diffuse through and numerous exposed pores, whereas FS-CuBTC$_{UM}$ has a surface that must be traversed due to the minimal interparticle voids and smaller pores. Kr, being the lighter element, passes through the surface much more easily and has a higher diffusivity once in the material, while Xe has a harder time entering the material and a lower diffusivity in the material. While both sorbates spend time in the tetragonal pores of the structure, Kr diffuses easily into

pores while Xe is typically held by the tetragonal pore much more readily.

The FS-CuBTC$_{UM}$ material, as elucidated by single adsorption isotherms and IAST calculations, establishes itself as a highly potent physisorbent with an unprecedented affinity for Kr, showing the capabilities of effectual separation from Kr/Xe mixtures under ambient conditions. Such reversed gas selectivity in densified MOFs has not been previously studied, observed, or reported. These findings motivated us to further investigate the potential of this material for practical Kr/Xe separation under ambient conditions using column break-through experiments for 1:1 and 1:10 Kr/Xe mixtures. Similar experiments were also performed on CuBTC$_{TWP}$ for a comparative study. As expected from the single adsorption isotherms, CuBTC$_{TWP}$ showed high Xe over Kr selectivity as indicated by the fast breakthrough of Kr and the retention of Xe in the bed filled with CuBTC$_{TWP}$. In contrast, Xe was not adsorbed and was detected by mass spectrometry shortly after the introduction of the Kr/Xe gas mixtures to the bed filled by FS-CuBTC$_{UM}$. Notably, Kr was retained in the bed (Figure 4A—D), confirming the potential of this material for efficient Kr/Xe separation. Kr can be regenerated from FS-CuBTC$_{UM}$ using an inert gas purge (helium, 20 sccm) or by applying a vacuum without the need of high temperature. Remarkably, the Kr breakthrough time remained consistently stable even after seven cycle tests (Figure 4E), attesting to the material's regeneration capability.

The unique separation properties of the material prompted us to investigate additional properties related to its practicality for Kr separation, such as mechanical properties and radiation resistance. In evaluating the practical efficiency of a material under extreme conditions such as exposure to γ radiation, two factors are considered: the chemical structure stability and the mechanical stability upon irradiation. The potential of FS-CuBTC$_{UM}$ as a radiation-resistant material was evaluated by exposure to γ radiation (^{60}Co source) from 0 kGy to 3500 kGy. The stability of the material was monitored by PXRD to confirm the retention of their crystallinity after γ irradiation (see the Supporting Information for experimental details and Figure S33). The material retains its crystallinity under a gamma irradiation of up to 3500 kGy. The γ radiation stability demonstrated here significantly exceeds the reported values for CuBTC.[38] The mechanical properties of FS-CuBTC$_{UM}$ were also monitored upon irradiation using the nanoindentation technique. The comparison of the mechanical properties between FS-CuBTC$_{UM}$ before irradiation, at 800 and at 1000 kGy, is shown in Figure 5. The hardness (H) and Young's modulus (E) values of 1180 ± 20 MPa and 23.5 ± 1.3 GPa, respectively, for FS-CuBTC$_{UM}$ indicate its superior mechanical properties compared with the reported CuBTC materials (pellets and monoliths). The most densified CuBTC monolith showed a density of 1.06 g cm^{-3} and mechanical properties of H = 460 ± 30 MPa, E = 9.3 ± 0.3 GPa.[39] The hardness of FS-CuBTC$_{UM}$, as demonstrated in this study, exceeds that of the most densely packed CuBTC previously reported by nearly 2.5 times, whereas the modulus is approximately double the value reported.[39] The high density and superior mechanical properties of this material could be attributed to the optimum packing of the FS-CuBTC particles and potential chemical connectivity between the particles through the defected site, as we explained earlier. The mechanical properties of the material were also studied after exposure of the material to 800 kGy of γ radiation. At this point, upon examination, the material maintained its stability in terms of physical shape (looked the same as the preradiated material; without visible sign of breakage) and retained its crystallinity as proven by PXRD. As mentioned earlier, FS-CuBTC$_{UM}$ retained its crystallinity and crystal structure after exposure to 1000 kGy of γ radiation; however, the hardness and Young's modulus of the material dropped by 10 and 23% to 1.06 ± 0.26 and 18.2 ± 3.2 GPa, respectively, with highly varied values between several areas of the sheet. This observation could be attributed to weakening of the intermolecular interactions between the individual nano-particles upon radiation. However, the material retained structural integrity without observable cracks even after exposure to radiation up to 3000 kGy. After FS-CuBTC was successfully produced using a commercially available paint sprayer, a noteworthy opportunity emerges for integrating this material into the nuclear energy sector. It proves to be an efficient and cost-effective multifunctional coating, enhancing leak prevention and functioning as an adsorbent material for the capture of Kr, all while avoiding the need for a container or column replacement, thereby offering an efficient and cost-effective solution.

CONCLUSIONS

In conclusion, our study introduces an innovative method to enhance Kr-selective adsorption in MOFs by controlling gas diffusion. We present a universal strategy for MOF densification by fine-tuning molecular-level interactions between the MOF nanoparticles. These chemical interactions facilitate bonding between neighboring crystallites, reducing intergranular voids and enhancing the physical and chemical properties of the MOFs, including mechanical strength, stability, and adsorption capabilities. Our approach uniquely combines reduced crystal size, the introduction of defects, and increased activation stress to achieve exceptional densification, along with enhanced framework flexibility. Reducing the size of MOF particles not only promotes close packing but also introduces structural flexibility, as fewer lattice units in smaller particles are highly responsive to external stress. The introduction of defects enhances particle interactions while altering the MOF's pore structure, rendering it more dynamic and amenable to deformation under stress. The activation process can impose stress on the MOF framework, optimizing crystal packing and influencing internal pore characteristics. In this scenario, a diffusion barrier for gases is established, allowing for the exceptional selective adsorption of Kr over Xe under ambient conditions. This is attributed to the smaller pore windows and minimal voids between particles, creating resistance that impedes the larger Xe from diffusing into the pore, while the lighter Kr can pass more rapidly into the pores. The potential of this method extends to enhancing the MOF quality and properties in bulk MOF syntheses, opening avenues for previously unattainable separation processes. Our ongoing work involves the application of this concept to a diverse range of MOFs, with the ultimate goal of transforming conventional MOFs into end-use products with extraordinary properties and applications.

EXPERIMENTAL SECTION

1. Synthesis of Gel CuBTC. Gel CuBTC was prepared by mixing 4 g of BTC ligand in 150 mL of ethanol with 6 g of copper(II) acetate monohydrate that was dissolved in a mixture of 150 mL of deionized water and 20 mL of acetic acid at ambient temperature. The sky-blue gel product was immediately transferred into centrifuge tubes and

centrifuged for 10 min at 8700 rpm. The gel product was washed, casted/processed, and activated in different ways to obtain the different forms of CuBTC presented herein.

2. Synthesis of CuBTC_{TWP} (TWP = Thoroughly Washed Powder). The sky-blue product of Gel CuBTC was resuspended and thoroughly washed several times with methanol and acetone with sonication and stirring followed by centrifugation after each wash until a transparent and colorless solution was attained. The solvent was decanted, and the sky-blue powder was left for 48 h to dry.

3. Synthesis of Monolithic CuBTC (Mono-CuBTC). The sky-blue product of Gel CuBTC was resuspended very well in ethanol (30 mL) in a centrifuge tube and recentrifuged for 10 min at 8700 rpm. The solvent was decanted, and the product was left to fully dry for 4−5 days until very dark shiny blue monolithic chunks were formed. Good resuspension is required to form a large high-quality, well-packed monolith. Poor resuspension leads to small monolithic pieces or inhomogeneous monoliths with light-blue agglomerates within the dark-blue chunks.

4. Synthesis of Flat Sheets CuBTC (FS-CuBTC). The sky-blue product of Gel CuBTC in the centrifuge tube was washed with ethanol, and the solvent was decanted. The product obtained was resuspended very well in ethanol (30 mL). The gel product was casted on glass in a closed glove bag saturated with ethanol to ensure an even and slow evaporation of solvent. The casted gel product was left to fully dry for 6−9 days depending on the casted amount until a dark shiny transparent film formed.

■ ASSOCIATED CONTENT

ⓢ Supporting Information

The Supporting Information is available free of charge at https://pubs.acs.org/doi/10.1021/acsami.4c01833.

The formation of MOF continuous coating using commercial paint sprayer (MP4)

The stability of the MOF flat sheets after soaking in ethanol for one month (MP4)

Materials processability; bulk density calculations; powder X-ray diffraction (PXRD); single-component gas adsorption measurements; surface area analysis; IAST selectivity calculation; krypton−xenon break-through experiments; kinetic study; evaluation of the mechanical properties; Gamma irradiation measurements; gas adsorption isotherms; pore size distribution; IAST selectivity; virial fitting; and Q_{st} curves (PDF)

■ AUTHOR INFORMATION

Corresponding Authors

Mona H. Mohamed − *Department of Chemistry, Illinois Institute of Technology, Chicago, Illinois 60616, United States; SE-MAT Smartly Engineered Materials LLC, Pittsburgh, Pennsylvania 15238, United States; Department of Chemistry, Faculty of Science, Alexandria University, Alexandria 5423021, Egypt*; Email: mmohamed3@iit.edu

Sameh K. Elsaidi − *Department of Chemistry, Illinois Institute of Technology, Chicago, Illinois 60616, United States; SE-MAT Smartly Engineered Materials LLC, Pittsburgh, Pennsylvania 15238, United States;* ⓞ orcid.org/0000-0002-8326-6984; Email: selsaidi@iit.edu

Authors

Islam Elzeny − *Department of Chemistry, Illinois Institute of Technology, Chicago, Illinois 60616, United States*

Joshua Samuel − *Department of Chemistry, Illinois Institute of Technology, Chicago, Illinois 60616, United States*

Yimeng Huang − *Department of Nuclear Science and Engineering, Massachusetts Institute of Technology, Cambridge, Massachusetts 02139, United States*

Ahmed S. Helal − *Department of Nuclear Science and Engineering, Massachusetts Institute of Technology, Cambridge, Massachusetts 02139, United States; Nuclear Materials Authority, Cairo 4710030, Egypt*

Mitchell Galanek − *Department of Nuclear Science and Engineering, Massachusetts Institute of Technology, Cambridge, Massachusetts 02139, United States*

Wenqian Xu − *X-ray Science Division, Advanced Photon Source, Argonne National Laboratory, Lemont, Illinois 60439, United States*

So Yeon Kim − *Department of Nuclear Science and Engineering, Massachusetts Institute of Technology, Cambridge, Massachusetts 02139, United States*

Tony Pham − *Department of Chemistry, University of South Florida, Tampa, Florida 33620, United States;* ⓞ orcid.org/0000-0001-5654-163X

Lenore Miller − *Department of Chemistry, North Carolina State University, Raleigh, North Carolina 27607, United States*

Adam Hogan − *Department of Chemistry, North Carolina State University, Raleigh, North Carolina 27607, United States*

Brian Space − *Department of Chemistry, North Carolina State University, Raleigh, North Carolina 27607, United States;* ⓞ orcid.org/0000-0003-0246-7408

Ju Li − *Department of Nuclear Science and Engineering and Department of Materials Science and Engineering, Massachusetts Institute of Technology, Cambridge, Massachusetts 02139, United States;* ⓞ orcid.org/0000-0002-7841-8058

Complete contact information is available at:
https://pubs.acs.org/10.1021/acsami.4c01833

Notes

The authors declare no competing financial interest.

■ ACKNOWLEDGMENTS

■ REFERENCES

(1) Banerjee, D.; Cairns, A. J.; Liu, J.; Motkuri, R. K.; Nune, S. K.; Fernandez, C. A.; Krishna, R.; Strachan, D. M.; Thallapally, P. K. Potential of metal−organic frameworks for separation of xenon and krypton. *Accounts of chemical research* **2015**, *48* (2), 211−219.

(2) Banerjee, D.; Simon, C. M.; Elsaidi, S. K.; Haranczyk, M.; Thallapally, P. K. Xenon Gas Separation and Storage Using Metal-Organic Frameworks. *Chem.* **2018**, *4* (3), 466−494.

(3) Chepel, V.; Araújo, H. Liquid noble gas detectors for low energy particle physics. *Journal of Instrumentation* **2013**, *8* (04), No. R04001.

(4) Undagoitia, T. M.; Rauch, L. Dark matter direct-detection experiments. *Journal of Physics G: Nuclear and Particle Physics* **2016**, *43* (1), No. 013001.

(5) Dobi, A.; Davis, C.; Hall, C.; Langford, T.; Slutsky, S.; Yen, Y. R. Detection of krypton in xenon for dark matter applications. *Nuclear Instruments and Methods in Physics Research Section A: Accelerators, Spectrometers, Detectors and Associated Equipment* **2011**, *665*, 1−6.

(6) Aprile, E.; Arisaka, K.; Arneodo, F.; Askin, A.; Baudis, L.; Behrens, A.; Brown, E.; Cardoso, J. M. R.; Choi, B.; Cline, D.; Fattori, S.; Ferella, A. D.; Giboni, K. L.; Kish, A.; Lam, C. W.; Lang, R. F.; Lim, K. E.; Lopes, J. A. M.; Marrodán Undagoitia, T.; Mei, Y.; Melgarejo Fernandez, A. J.; Ni, K.; Oberlack, U.; Orrigo, S. E. A.; Pantic, E.; Plante, G.; Ribeiro, A. C. C.; Santorelli, R.; dos Santos, J. M. F.; Schumann, M.; Shagin, P.; Teymourian, A.; Tziaferi, E.; Wang, H.; Yamashita, M. The XENON100 dark matter experiment. *Astropart. Phys.* **2012**, *35* (9), 573−590.

(7) Murra, M. Removal of noble gases from xenon by cryogenic distillation. *Verh. Dtsch. Phys. Ges.* **2018**, No. 50010614.

(8) Bohnenstingl, J.; Heidendael, M.; Laser, M.; Mastera, S.; Merz, E. *Cryogenic separation of krypton and xenon from dissolver off-gas*; International Atomic Energy Agency 1976.

(9) Wang, Q.; Xiong, S. S.; Xiang, Z. H.; Peng, S. M.; Wang, X. L.; Cao, D. P. Dynamic separation of Xe and Kr by metal-organic framework and covalent-organic materials: a comparison with activated charcoal. *SCIENCE CHINA-CHEMISTRY* **2016**, *59* (5), 643−650.

(10) Simon, C. M.; Mercado, R.; Schnell, S. K.; Smit, B.; Haranczyk, M. What Are the Best Materials To Separate a Xenon/Krypton Mixture? *CHEMISTRY OF MATERIALS* **2015**, *27* (12), 4459−4475.

(11) Elsaidi, S. K.; Mohamed, M. H.; Simon, C. M.; Braun, E.; Pham, T.; Forrest, K. A.; Xu, W.; Banerjee, D.; Space, B.; Zaworotko, M. J.; Thallapally, P. K. Effect of ring rotation upon gas adsorption in SIFSIX-3-M (M = Fe, Ni) pillared square grid networks. *Chemical Science* **2017**, *8* (3), 2373−2380.

(12) Mohamed, M. H.; Elsaidi, S. K.; Pham, T.; Forrest, K. A.; Schaef, H. T.; Hogan, A.; Wojtas, L.; Xu, W.; Space, B.; Zaworotko, M. J.; Thallapally, P. K. Hybrid Ultra-Microporous Materials for Selective Xenon Adsorption and Separation. *Angew. Chem., Int. Ed.* **2016**, *55* (29), 8285−8289.

(13) Elsaidi, S. K.; Mohamed, M. H.; Helal, A. S.; Galanek, M.; Pham, T.; Suepaul, S.; Space, B.; Hopkinson, D.; Thallapally, P. K.; Li, J. Radiation-resistant metal-organic framework enables efficient separation of krypton fission gas from spent nuclear fuel. *Nat. Commun.* **2020**, *11* (1), 3103.

(14) Chui, S. S. Y.; Lo, S. M. F.; Charmant, J. P. H.; Orpen, A. G.; Williams, I. D. A Chemically Functionalizable Nanoporous Material [Cu3(TMA)2(H2O)3]n. *Science* **1999**, *283* (5405), 1148−1150.

(15) Hou, J.; Sapnik, A. F.; Bennett, T. D. Metal−organic framework gels and monoliths. *Chemical Science* **2020**, *11* (2), 310−323.

(16) Qi, X.; Liu, K.; Chang, Z. Beyond powders: Monoliths on the basis of metal-organic frameworks (MOFs). *Chemical Engineering Journal* **2022**, *441*, No. 135953.

(17) Wang, Z.; Liu, L.; Li, Z.; Goyal, N.; Du, T.; He, J.; Li, G. K. Shaping of metal−organic frameworks: a review. *Energy Fuels* **2022**, *36* (6), 2927−2944.

(18) Mohamed, M. H.; Elzeny, I.; Samuel, J.; Xu, W.; Malliakas, C. D.; Picard, Y. N.; Pham, T.; Miller, L.; Hogan, A.; Space, B.; Hopkinson, D.; Elsaidi, S. K. Turning Normal to Abnormal: Reversing CO2/C2-Hydrocarbon Selectivity in HKUST-1. *Adv. Funct. Mater.* **2024**, *n/a* (n/a), No. 2312280.

(19) Dhainaut, J.; Avci-Camur, C.; Troyano, J.; Legrand, A.; Canivet, J.; Imaz, I.; Maspoch, D.; Reinsch, H.; Farrusseng, D. Systematic study of the impact of MOF densification into tablets on textural and mechanical properties. *CrystEngComm* **2017**, *19* (29), 4211−4218.

(20) Bennett, T. D.; Cheetham, A. K.; Fuchs, A. H.; Coudert, F.-X. Interplay between defects, disorder and flexibility in metal-organic frameworks. *Nat. Chem.* **2017**, *9* (1), 11−16.

(21) Yuan, S.; Sun, X.; Pang, J.; Lollar, C.; Qin, J.-S.; Perry, Z.; Joseph, E.; Wang, X.; Fang, Y.; Bosch, M.; Sun, D.; Liu, D.; Zhou, H.-C. PCN-250 under Pressure: Sequential Phase Transformation and the Implications for MOF Densification. *Joule* **2017**, *1* (4), 806−815.

(22) Shimizu, G. K. How Much Pressure Is Too Much Pressure for a MOF? *Chem.* **2017**, *3* (6), 924−925.

(23) Bennett, T. D.; Simoncic, P.; Moggach, S. A.; Gozzo, F.; Macchi, P.; Keen, D. A.; Tan, J.-C.; Cheetham, A. K. Reversible pressure-induced amorphization of a zeolitic imidazolate framework (ZIF-4). *Chem. Commun.* **2011**, *47* (28), 7983−7985.

(24) Widmer, R. N.; Lampronti, G. I.; Chibani, S.; Wilson, C. W.; Anzellini, S.; Farsang, S.; Kleppe, A. K.; Casati, N. P. M.; MacLeod, S. G.; Redfern, S. A. T.; Coudert, F.-X.; Bennett, T. D. Rich Polymorphism of a Metal−Organic Framework in Pressure−Temperature Space. *J. Am. Chem. Soc.* **2019**, *141* (23), 9330−9337.

(25) Yot, P. G.; Ma, Q.; Haines, J.; Yang, Q.; Ghoufi, A.; Devic, T.; Serre, C.; Dmitriev, V.; Férey, G.; Zhong, C.; Maurin, G. Large breathing of the MOF MIL-47(VIV) under mechanical pressure: a joint experimental−modelling exploration. *Chemical Science* **2012**, *3* (4), 1100−1104.

(26) Binns, J.; Kamenev, K. V.; Marriott, K. E. R.; McIntyre, G. J.; Moggach, S. A.; Murrie, M.; Parsons, S. A non-topological mechanism for negative linear compressibility. *Chem. Commun.* **2016**, *52* (47), 7486−7489.

(27) Graham, A. J.; Banu, A.-M.; Düren, T.; Greenaway, A.; McKellar, S. C.; Mowat, J. P. S.; Ward, K.; Wright, P. A.; Moggach, S. A. Stabilization of Scandium Terephthalate MOFs against Reversible Amorphization and Structural Phase Transition by Guest Uptake at Extreme Pressure. *J. Am. Chem. Soc.* **2014**, *136* (24), 8606−8613.

(28) Ryder, M. R.; Civalleri, B.; Bennett, T. D.; Henke, S.; Rudić, S.; Cinque, G.; Fernandez-Alonso, F.; Tan, J.-C. Identifying the Role of Terahertz Vibrations in Metal-Organic Frameworks: From Gate-Opening Phenomenon to Shear-Driven Structural Destabilization. *Phys. Rev. Lett.* **2014**, *113* (21), No. 215502.

(29) Mason, J. A.; Oktawiec, J.; Taylor, M. K.; Hudson, M. R.; Rodriguez, J.; Bachman, J. E.; Gonzalez, M. I.; Cervellino, A.; Guagliardi, A.; Brown, C. M.; Llewellyn, P. L.; Masciocchi, N.; Long, J. R. Methane storage in flexible metal−organic frameworks with intrinsic thermal management. *Nature* **2015**, *527* (7578), 357−361.

(30) Tan, J.-C. *Mechanical Behaviour of Metal−Organic Framework Materials*; Royal Society of Chemistry: 2023.

(31) Cui, J.; Qiu, Z.; Yang, L.; Zhang, Z.; Cui, X.; Xing, H. Kinetic-Sieving of Carbon Dioxide from Acetylene through a Novel Sulfonic Ultramicroporous Material. *Angew. Chem., Int. Ed.* **2022**, *61* (39), No. e202208756.

(32) Wang, Y.; Zhao, D. Beyond Equilibrium: Metal−Organic Frameworks for Molecular Sieving and Kinetic Gas Separation. *Cryst. Growth Des.* **2017**, *17* (5), 2291−2308.

(33) Wang, X.; Ma, F.; Liu, S.; Chen, L.; Xiong, S.; Dai, X.; Tai, B.; He, L.; Yuan, M.; Mi, P.; Gong, S.; Li, G.; Tao, Y.; Wan, J.; Chen, L.; Sun, X.; Tang, Q.; He, L.; Yang, Z.; Chai, Z.; Wang, S. Thermodynamics-Kinetics-Balanced Metal−Organic Framework for In-Depth Radon Removal under Ambient Conditions. *J. Am. Chem. Soc.* **2022**, *144* (30), 13634−13642.

(34) Fernandez, C. A.; Liu, J.; Thallapally, P. K.; Strachan, D. M. Switching Kr/Xe Selectivity with Temperature in a Metal−Organic Framework. *J. Am. Chem. Soc.* **2012**, *134* (22), 9046−9049.

(35) Kim, H.; Choe, J. H.; Kang, M.; Kang, D. W.; Yun, H.; Youn, J.; Lee, W.; Lee, J.; Hong, C. S. Switchable Xe/Kr Selectivity in a Hofmann-Type Metal−Organic Framework via Temperature-Responsive Rotational Dynamics. *Small* **2023**, *19* (35), No. 2301905.

(36) Xiong, X. L.; Chen, G. H.; Xiao, S. T.; Ouyang, Y. G.; Li, H. B.; Wang, Q. New Discovery of Metal-Organic Framework UTSA-280: Ultrahigh Adsorption Selectivity of Krypton over Xenon. *JOURNAL OF PHYSICAL CHEMISTRY C* **2020**, *124* (27), 14603−14612.

(37) Vahdat, M. T.; Campi, D.; Colonna, N.; Villalobos, L. F.; Marzari, N.; Agrawal, K. V. Efficient Kr/Xe separation from triangular g-C(3)N(4)nanopores, a simulation study. *JOURNAL OF MATERIALS CHEMISTRY A* **2020**, *8* (34), 17747−17755.

(38) Volkringer, C.; Falaise, C.; Devaux, P.; Giovine, R.; Stevenson, V.; Pourpoint, F.; Lafon, O.; Osmond, M.; Jeanjacques, C.; Marcillaud, B.; Sabroux, J. C.; Loiseau, T. Stability of metal−organic frameworks under gamma irradiation. *Chem. Commun.* **2016**, *52* (84), 12502−12505.

(39) Tian, T.; Zeng, Z.; Vulpe, D.; Casco, M. E.; Divitini, G.; Midgley, P. A.; Silvestre-Albero, J.; Tan, J.-C.; Moghadam, P. Z.; Fairen-Jimenez, D. A sol−gel monolithic metal−organic framework with enhanced methane uptake. *Nat. Mater.* **2018**, *17* (2), 174−179.